Comparison of Cartesian grid configurations for application of the finite-difference time-domain method to electromagnetic scattering by dielectric particles

Ping Yang, George W. Kattawar, Kuo-Nan Liou, and Jun Q. Lu

Two grid configurations can be employed to implement the finite-difference time-domain (FDTD) technique in a Cartesian system. One configuration defines the electric and magnetic field components at the cell edges and cell-face centers, respectively, whereas the other reverses these definitions. These two grid configurations differ in terms of implication on the electromagnetic boundary conditions if the scatterer in the FDTD computation is a dielectric particle. The permittivity has an abrupt transition at the cell interface if the dielectric properties of two adjacent cells are not identical. Similarly, the discontinuity of permittivity is also observed at the edges of neighboring cells that are different in terms of their dielectric constants. We present two FDTD schemes for light scattering by dielectric particles to overcome the above-mentioned discontinuity on the basis of the electromagnetic boundary conditions for the two Cartesian grid configurations. We also present an empirical approach to accelerate the convergence of the discrete Fourier transform to obtain the field values in the frequency domain. As a new application of the FDTD method, we investigate the scattering properties of multibranched bullet-rosette ice crystals at both visible and thermal infrared wavelengths. © 2004 Optical Society of America

OCIS codes: 010.1290, 010.3920, 010.1310, 290.5850, 290.1310, 280.1310.

1. Introduction

The scattering and absorption properties of small dielectric nonspherical particles are essential elements for the implementation of various passive and active remote sensing techniques for atmospheric applications and for the simulation of radiative transfer in the coupled Earth–atmosphere system.[1,2] A number of rigorous and approximate methods have been developed to investigate physical processes associated with the electromagnetic scattering by nonspherical and inhomogeneous particles; the strengths and weaknesses of these methods have recently been reviewed by Mishchenko *et al.*[2] and Kahnert.[3]

The finite-difference time-domain (FDTD) method pioneered by Yee[4] in 1966 and subsequently developed by numerous electrical engineers and computational physicists (e.g., Taflove and colleagues,[5,6] Kunz and Luebbers[7]) has been shown to be flexible and robust in electromagnetic scattering problems. It has been widely applied to problems as diverse as the analysis of antenna performance and the assessment of bioelectromagnetic hazards.[5] The FDTD method has also been used to compute the scattering properties of nonspherical and inhomogeneous ice crystals and aerosols in the terrestrial atmosphere.[8–14] The popularity of this method can be recognized from the wealth of relevant publications, as recently surveyed by Shlager and Schneider.[15]

Although substantial theoretical developments and modeling efforts have been focused on the implementation of the FDTD method in various curvilinear coordinate systems,[6,16] the most straightforward implementation of this method has been use of the Cartesian grid meshes. When the time-dependent Maxwell's curl equations are discretized in a Cartesian system by use of the leapfrog difference (or the

P. Yang (pyang@ariel.met.tamu.edu) is with the Department of Atmospheric Sciences, TAMU 3150, Texas A&M University, College Station, Texas 77843-3150. G. W. Kattawar is with the Department of Physics, Texas A&M University, 4242 TAMU, College Station, Texas 77843-4252. K.-N. Liou is with the Department of Atmospheric Sciences, University of California at Los Angeles, Los Angeles, California 90095-1565. J. Q. Lu is with the Department of Physics, East Carolina University, Greenville, North Carolina 27858.

central-difference) technique, there are two numerical schemes used to specify the spatial location of the electric and magnetic fields. In one of the two schemes the Cartesian components of the electric field are defined at the centers of the cell faces, whereas the corresponding components of the magnetic field are defined at the cell edges. In the other scheme, one simply interchanges the electric and magnetic fields. These two schemes differ in terms of their implication on the electromagnetic boundary conditions if the dielectric characteristics of adjacent cells are not identical (e.g., in the case in which the cells are located at the particle surface).

The objective of this study is first to derive appropriate FDTD schemes associated with the above-mentioned Cartesian grid configurations to circumvent the indeterminate nature of the permittivity and field values at the location where the medium dielectric properties are discontinuous. Second, on the basis of the present FDTD schemes, the scattering computations are carried out to assess the numerical accuracy associated with the two different Cartesian grid configurations. Third, we present a simple and yet efficient numerical method to improve the convergence of the electric field in the frequency domain. Finally, as a new application, we use the FDTD method to study the effect of the multibranches of bullet-rosette ice crystals on the optical characteristics of these particles. Note that the scattering and absorption properties of bullet-rosette ice crystals are important in the study of the radiative properties of cirrus clouds in the atmosphere.

This paper is organized as follows. In Section 2 we provide the theoretical basis for the two Cartesian FDTD schemes that can be applied to the case involving a discontinuity of dielectric properties. In Section 3 we illustrate that the convergence of near-field signals in the frequency domain is generally slow, and we present a method to improve the rate of convergence. In Section 4 we show the performance comparison of the two FDTD schemes developed in Section 2, including cases for cubes and spherical particles with moderate and large complex refractive indices. Presented in Section 4 are also the phase matrices of various types of bullet-rosette ice crystals. Finally, conclusions are given in Section 5.

2. Cartesian Grid for the Implementation of the Finite-Difference Time-Domain Method

For the implementation of the FDTD technique in a Cartesian system, Yee's scheme[4] involving the second-order finite-difference analog of Maxwell's curl equations has been most popular, although several higher-order schemes have also been suggested.[5] Figure 1(a) shows Yee's original grid configuration for the location of the electric and magnetic field vector components on a cubic cell. Figure 1(b) shows an alternative of Yee's grid configuration. Note that the grid configuration in Fig. 1(b) is also referred to as Yee's scheme in the literature.[6] It is evident from Fig. 1 that these two grid configurations differ by a spatial shift of $(\Delta x, \Delta y, \Delta z) = (\Delta s/2, \Delta s/2, \Delta s/2)$, as-
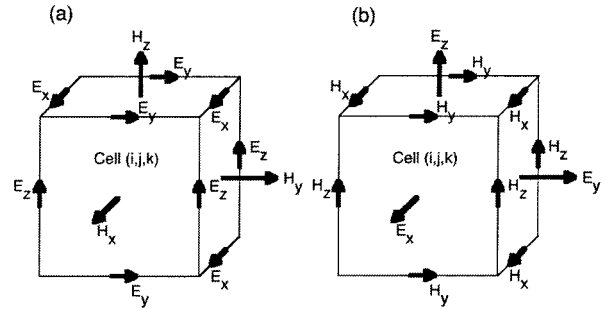

Fig. 1. Two Cartesian grid configurations used to implement the FDTD method. The configuration in (a) was originally reported by Yee in 1966.

suming a uniform grid size along the x, y, and z axes. Because of a half-step spatial shift, the two grid configurations, if applied to the electromagnetic scattering by a dielectric particle, are different in terms of their implication on the electromagnetic boundary conditions. For the cells intersecting with the particle surface (i.e., the dielectric properties of adjacent cells are different), these two grid configurations lead to two versions of the finite-difference equations when we are dealing with the discontinuity of medium dielectric properties, as discussed below.

Consider the electromagnetic scattering by a nonferromagnetic dielectric particle. The Maxwell curl equations for the physical process are given as follows:

$$\frac{\partial \mathbf{E}(\mathbf{r}, t)}{\partial t} = \frac{c}{\varepsilon} \nabla \times \mathbf{H}(\mathbf{r}, t), \qquad (1)$$

$$\frac{\partial \mathbf{H}(\mathbf{r}, t)}{\partial t} = -c \nabla \times \mathbf{E}(\mathbf{r}, t), \qquad (2)$$

where ε is the complex permittivity of the dielectric medium of which the particle is composed and c is the speed of light in vacuum. To avoid complex variables in the FDTD numerical computation, Eq. (1) can be transformed to a form given by[8]

$$\frac{\partial [\exp(\omega t \varepsilon_i / \varepsilon_r) \mathbf{E}(\mathbf{r}, t)]}{\partial t} = \exp(\omega t \varepsilon_i / \varepsilon_r) \frac{c}{\varepsilon_r} \nabla \times \mathbf{H}, \quad (3)$$

where ε_r and ε_i are the real and imaginary parts of the permittivity, respectively, and ω is the angular frequency of the incident wave. We can use the leapfrog finite-difference scheme to discretize Eqs. (2) and (3) with respect to time in a straightforward manner as follows:

$$\mathbf{H}^{n+1/2}(\mathbf{r}) = \mathbf{H}^{n-1/2}(\mathbf{r}) - c \Delta t \nabla \times \mathbf{E}^n(\mathbf{r}), \qquad (4)$$

$$\mathbf{E}^{n+1}(\mathbf{r}) = \exp[-\tau(\mathbf{r}) \Delta t] \mathbf{E}^n(\mathbf{r})$$
$$+ \exp[-\tau(\mathbf{r}) \Delta t / 2] \frac{c \Delta t}{\varepsilon_r} \nabla \times \mathbf{H}^{n+1/2}(\mathbf{r}),$$
$$(5)$$

where $\tau(\mathbf{r}) = \omega\varepsilon_i(\mathbf{r})/\varepsilon_r(\mathbf{r})$ and the superscripts in Eqs. (4) and (5) denote the time steps. The temporal discretization from Eqs. (2) and (3) to Eqs. (4) and (5) does not pose any difficulty in practice because the electric and magnetic fields are continuous functions in time. However, a careful consideration is required to discretize Eqs. (4) and (5) with respect to the spatial dependence of the electric and magnetic fields.

As an example, let us consider the z component of Eq. (5) and apply the leapfrog difference scheme to discretize the corresponding differential equation. Employing the grid configuration in Fig. 1(b), we obtain the following finite-difference equation:

$$
\begin{aligned}
E_z^{n+1}(i, j, k + 1/2) ={}& \exp[-\tau(i,j,k+1/2)\Delta t] \\
& \times E_z^n(i, j, k + 1/2) \\
& + \exp[-\tau(i, j, k + 1/2)\Delta t/2] \\
& \times \frac{c\Delta t}{\varepsilon_r(i, j, k + 1/2)\Delta s} \\
& \times [H_x^{n+1/2}(i, j - 1/2, k + 1/2) \\
& - H_x^{n+1/2}(i, j + 1/2, k + 1/2) \\
& + H_y^{n+1/2}(i + 1/2, j, k + 1/2) \\
& - H_y^{n+1/2}(i - 1/2, j, k + 1/2)],
\end{aligned}
\tag{6}
$$

where $\tau(i, j, k + 1/2) = \omega\varepsilon_i(i, j, k + 1/2)/\varepsilon_r(i, j, k + 1/2)$. The quantities $\varepsilon_r(i, j, k + 1/2)$ and $\varepsilon_i(i, j, k + 1/2)$ are the values of the real and imaginary parts of the permittivity at the location $(x, y, z) = (i, j, k + 1/2)\Delta s$. If two grid cells with an interface at $(x, y, z) = (i, j, k + 1/2)\Delta s$ are different, the permittivity is undefined. This can be well illustrated for the case in which the scattering particle is a cube that conforms to a Cartesian FDTD grid mesh. Figure 2 shows a side view (along the x-axis direction) of a cubic particle embedded in a Cartesian grid mesh. On the particle surface, the E_z and E_y components are specified at the locations marked as X and O, respectively. Evidently, the permittivity is not continuous at these locations. If the local values of the permittivity are used by a brute force approach, then it is not certain whether the permittivity of the surroundings (i.e., vacuum in the present case) or that of the particle should be used at the particle surface. In addition to the difficulty associated with how to uniquely define the permittivity at the particle surface, the electric field vector components cannot be defined on the particle surface either if the grid configuration specified in Fig. 1(b) is employed. This is because an electric field component normal to the particle surface is discontinuous. Therefore there is a need to address the issue regarding the discretization of the Maxwell equations with respect to space for the FDTD application in the case in which the scatterer of interest is a dielectric particle. It should be pointed out that a previous study by Pregla and Pascher[17] already addressed the issue concerning the specification of the dielectric constants in discrete
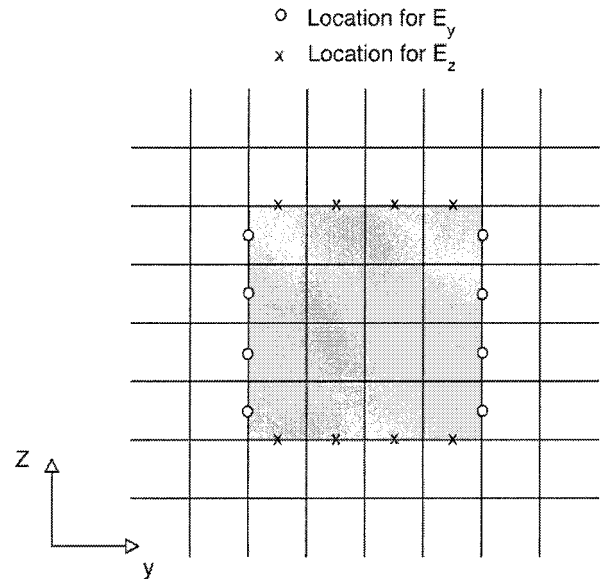

Fig. 2. Side view of a cubic particle that is embedded in a Cartesian FDTD grid mesh. The electric field components normal to the particle surface cannot be defined at the locations marked X and O in the diagram because of the discontinuity of the field components at these locations.

numerical computation (specifically, the method of lines in their study) at a location where an abrupt transition of medium dielectric properties is present.

According to the nature of discrete numerical computation, the basic spatial unit in the finite-difference scheme is the grid cell. It is unlikely to resolve any subcell-scale variation of a variable in the FDTD calculation. Thus a scattering particle in the Cartesian FDTD implementation must be approximated by a number of grid cells. For example, a pseudosphere composed of a number of cubic cells is used as a surrogate to approximate a sphere in the FDTD computation. The dielectric properties of these cells in the FDTD grid mesh can be different, i.e., one can have colored cells in terms of their permittivities. However, for a given cell, the dielectric properties must be homogeneous throughout the cell. This approximation leads to the well-known staircasing effect in the Cartesian FDTD implementation. Many approaches have been suggested to reduce the staircasing effect (e.g., Taflove and Hagness[6] and the references cited therein).

Under the condition that a particle is approximated by a number of homogeneous cells in the FDTD calculation, we can derive two appropriate FDTD numerical schemes associated with the grid configurations in Figs. 1(a) and 1(b). First, let us consider the general electromagnetic boundary conditions given by[18]

$$
\mathbf{n} \times (\mathbf{E}^+ - \mathbf{E}^-) = 0, \tag{7a}
$$

$$
\mathbf{n} \times (\mathbf{H}^+ - \mathbf{H}^-) = \mathbf{K}, \tag{7b}
$$

$$
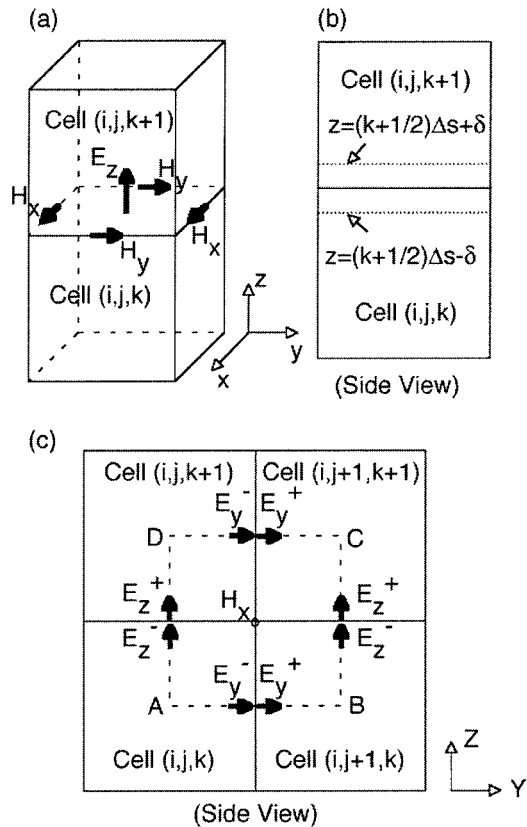\mathbf{n} \cdot (\mathbf{D}^+ - \mathbf{D}^-) = \rho_s, \tag{7c}
$$

Fig. 3. Electric and magnetic fields associated with two adjacent cells that are not identical in terms of their dielectric constants.

where **n** is a unit vector normal to the interface, **D** is the electric displacement vector given by $\varepsilon\mathbf{E}$ in which ε is the permittivity, **K** is the surface current density, and ρ_s is the surface density of free charge. For the electromagnetic scattering by a dielectric particle, we have $\mathbf{K} = 0$ because a finite conductivity cannot sustain $\mathbf{K}$.[19] In addition, we have $\rho_s = 0$ for a dielectric particle. Thus the tangential components of the electric and magnetic fields are continuous across the cell interface whereas the normal component of electric displacement is continuous at the cell interface. Evidently the grid configuration in Fig. 1(a) implicitly satisfies the electromagnetic boundary condition because the electric and magnetic components involved in this grid configuration are continuous, although a discontinuity of permittivity may exist at cell faces or edges. On the contrary, for the grid configuration in Fig. 1(b), the normal components of the electric field vectors at the centers of cell faces have abrupt transitions, although the corresponding components of the electric displacement vectors are continuous at these locations if the dielectric constants of adjacent cells are not identical.

Consider two adjacent homogeneous cells with field locations given by the configuration shown in Fig. 3. The permittivity for the upper cell centered at $(x, y, z) = (i, j, k + 1)\Delta s$ is denoted as $\varepsilon_{i,j,k+1}$, whereas the permittivity for the lower cell is given

by $\varepsilon_{i,j,k}$. Consider the E_z component at the cell interface. At the plane of $z = (k + 1/2)\Delta s + \delta$ with $\delta \to 0$ (i.e., the upper-cell side of the cell interface), the spatial discretization of Eq. (1) for the E_z components leads to the following differential–difference equation:

$$\frac{\partial E_z^+(i, j, k + 1/2, t)}{\partial t} = \frac{c}{\varepsilon_{i,j,k+1}\Delta s}[H_x^+(i, j - 1/2, k + 1/2, t)$$
$$- H_x^+(i, j + 1/2, k + 1/2, t)$$
$$+ H_y^+(i + 1/2, j, k + 1/2, t)$$
$$- H_y^+(i - 1/2, j, k + 1/2, t)],$$
(8)

where the superscript $+$ indicates that the associated variables are evaluated at the upper-cell side of the interface, e.g., $E_z^+(i, j, k + 1/2)$ implies that the value of $E_z(x, y, z, t)$ is evaluated at $(x, y, z) = [i\Delta s, j\Delta s, (k + 1/2)\Delta s + \delta]$ with $\delta \to 0$.

Similarly, at the lower-cell side of the cell interface [i.e., the plane of $z = (k + 1/2)\Delta s - \delta$ with $\delta \to 0$], we have

$$\frac{\partial E_z^-(i, j, k + 1/2, t)}{\partial t} = \frac{c}{\varepsilon_{i,j,k}\Delta s}[H_x^-(i, j - 1/2, k + 1/2, t)$$
$$- H_x^-(i, j + 1/2, k + 1/2, t)$$
$$+ H_y^-(i + 1/2, j, k + 1/2, t)$$
$$- H_y^-(i - 1/2, j, k + 1/2, t)],$$
(9)

where the superscript $-$ indicates that the associated variables are evaluated at the lower-cell side of the interface, e.g., $E_z^-(i, j, k + 1/2)$ implies that the value of $E_z(x, y, z, t)$ is evaluated at $(x, y, z) = [i\Delta s, j\Delta s, (k + 1/2)\Delta s - \delta]$ with $\delta \to 0$. Because the tangential components of the magnetic field vector components are continuous, we must have

$$H_x^+(i, j \pm 1/2, k + 1/2, t) = H_x^-(i, j \pm 1/2, k + 1/2, t),$$
(10a)

$$H_y^+(i \pm 1/2, j, k + 1/2, t) = H_y^-(i \pm 1/2, j, k + 1/2, t).$$
(10b)

On the contrary, the normal components of the electric field are not continuous at the cell interface, that is,

$$E_z^+(i, j, k + 1/2, t) \neq E_z^-(i, j, k + 1/2, t). \quad (11)$$

To obtain an appropriate FDTD scheme to compute the electric field at the cell interface, we define the following averaged quantities:

$$E_z(i, j, k + 1/2, t) = [E_z{}^+(i, j, k + 1/2, t)$$
$$+ E_z{}^-(i, j, k + 1/2, t)]/2 \,,$$

(12a)

$$\frac{1}{\varepsilon(i, j, k + 1/2)} = \frac{1}{2}\left(\frac{1}{\varepsilon_{i,j,k}} + \frac{1}{\varepsilon_{i,j,k+1}}\right).$$ (12b)

With the auxiliary quantities defined in Eqs. (12a) and (12b), averaging Eqs. (8) and (9), we have

$$\frac{\partial E_z(i, j, k + 1/2, t)}{\partial t} = \frac{c}{\varepsilon(i, j, k + 1/2)\Delta s}[H_x(i, j$$
$$- 1/2, k + 1/2, t)$$
$$- H_x(i, j + 1/2, k + 1/2, t)$$
$$+ H_y(i + 1/2, j, k + 1/2, t)$$
$$- H_y(i - 1/2, j, k + 1/2, t)].$$

(13)

Using the approach suggested by Yang and Liou,[8] we can then transform Eq. (13) to a real form to avoid complex computation in the numerical implementation as follows:

area *ABCD* in Fig. 3(c) and subsequently applying the Stokes formula, we obtain

$$\frac{\partial H_x(i, j + 1/2, k + 1/2)}{\partial t} = -\frac{c}{\Delta s^2}$$
$$\times \left[\int_A^B E_y(x, y, z, t)\mathrm{d}y\right.$$
$$+ \int_B^c E_z(x, y, z, t)\mathrm{d}z$$
$$+ \int_c^D E_y(x, y, z, t)\mathrm{d}y$$
$$\left.+ \int_D^A E_z(x, y, z, t)\mathrm{d}z\right].$$

(15)

To further discretize Eq. (15), we consider, as an example, the fourth term on the right-hand side of Eq. (15) as follows:

$$\frac{1}{\Delta s^2}\left[\int_D^A E_z(x, y, z, t)\mathrm{d}z = \frac{1}{\Delta s^2}[E_z{}^-(i, j, k + 1/2)\right.$$
$$\times \Delta s/2 + E_z{}^+(i, j, k + 1/2)\Delta s/2]$$
$$= -\frac{1}{\Delta s}E_z(i, j, k + 1/2).$$

(16)

$$\frac{\partial\{\exp[i\omega\varepsilon_i(i, j, k + 1/2)/\varepsilon_r(i, j, k + 1/2)]E_z(i, j, k + 1/2, t)\}}{\partial t}$$

$$= \exp[i\omega\varepsilon_i(i, j, k + 1/2)/\varepsilon_r(i, j, k + 1/2)]\frac{c}{\varepsilon_r(i, j, k + 1/2)\Delta s}[H_x(i, j - 1/2, k + 1/2, t)$$

$$- H_x(i, j + 1/2, k + 1/2, t) + H_y(i + 1/2, j, k + 1/2, t) - H_y(i - 1/2, j, k + 1/2, t)], \quad (14)$$

where $\varepsilon_i(i, j, k + 1/2)$ and $\varepsilon_r(i, j, k + 1/2)$ are the imaginary and real parts of the averaged permittivity defined in Eq. (12b), respectively. Equation (14) can be further discretized with respect to time, leading to a finite-difference scheme that is in the same form as Eq. (6). However, the permittivity and electric field involved in the finite-difference equation cannot be understood as their local values but the average of the field components at the two sides of the cell interface. Therefore, if one uses the grid configuration in Fig. 1(b), the average of the electric field is mandatory so that the electromagnetic boundary conditions are valid. The finite-difference equation to compute the magnetic field involves the Cartesian components of the electric field that must be the averaged values as well. From Figs. (3a) and (3c), after integrating the *x* components of Eq. (2) over the

Similarly, the other three terms on the right-hand side of Eq. (15) can be given by the averaged electric field vector component. Thus we have

$$H_x{}^{n+1/2}(i, j + 1/2, k + 1/2)$$
$$= H_x{}^{n-1/2}(i, j + 1/2, k + 1/2)$$
$$- \frac{c\Delta t}{\Delta s}[E_y{}^n(i, j + 1/2, k) - E_y{}^n(i, j + 1/2, k + 1)$$
$$+ E_z{}^n(i + 1, j, k + 1/2) - E_z{}^n(i, j, k + 1/2)]. \quad (17)$$

Therefore, if we employ the grid configuration specified in Fig. 1(b), the appropriate FDTD scheme for E_z and H_x, for example, are given by Eqs. (6) and (17) in which the electric field and permittivity do not posses the conventional meanings as given by their local values. It is clear that the difficulty associated with

the medium discontinuity when the scatterer is a dielectric particle has been circumvented in the preceding scheme.

In the FDTD simulation for the scattering properties of a particle, the near field must be mapped to its far-field counterpart. If we employ the volume-integral-based approach,[8] we are required to determine the electric field at the centers of the cells from which the scattering particle is composed. Consider E_z as an example. We have the following electromagnetic boundary condition at the cell interface shown in Fig. 3(c):

$$\varepsilon_{i,j,k+1}E_z^+(i, j, k + 1/2) = \varepsilon_{i,j,k}E_z^-(i, j, k + 1/2). \tag{18}$$

Using Eqs. (12a) and (18), we obtain

$$E_z^+(i, j, k + 1/2) = \frac{2\varepsilon_{i,j,k}}{\varepsilon_{i,j,k} + \varepsilon_{i,j,k+1}} E_z(i, j, k + 1/2), \tag{19a}$$

$$E_z^-(i, j, k + 1/2) = \frac{2\varepsilon_{i,j,k}}{\varepsilon_{i,j,k} + \varepsilon_{i,j,k+1}} E_z(i, j, k + 1/2). \tag{19b}$$

Thus the z component of the electric field at the cell center (i, j, k) is given by

$$E_z(i, j, k) = \left[\frac{\varepsilon_{i,j,k+1}}{\varepsilon_{i,j,k} + \varepsilon_{i,j,k+1}} E_z(i, j, k + 1/2) \right.$$
$$\left. + \frac{\varepsilon_{i,j,k-1}}{\varepsilon_{i,j,k} + \varepsilon_{i,j,k-1}} E_z(i, j, k - 1/2) \right]. \tag{20}$$

The preceding expressions, i.e., Eqs. (6), (12a), (12b), (17), and (20), form the FDTD algorithm for the grid configuration in Fig. 1(b). Similarly, if we use the grid configuration in Fig. 1(a), the spatial discretization for the electric field for the E_z component, for example, is given by

An important point to note is that in Eq. (21) the electric field component E_z is a local value. Thus, if we use Yee's original grid configuration [Fig. 1(a)], only the permittivity needs to be averaged in the FDTD algorithm to deal with the medium discontinuity. For the FDTD scheme given by Eq. (21), the electric field components at the cell centers in the case of E_z, for example, can be obtained in a straightforward manner as follows:

$$E_z(i, j, k) = [E_z(i - 1/2, j - 1/2, k)$$
$$+ E_z(i + 1/2, j - 1/2, k)$$
$$+ E_z(i + 1/2, j + 1/2, k)$$
$$+ E_z(i - 1/2, j + 1/2, k)]/4. \tag{23}$$

The expressions in Eqs. (20) and (23) give the electric field components at cell centers for the grid configurations shown in Figs. 1(a) and 1(b). Sun and Fu,[11] who used the grid configuration in Fig. 1(b), reported a useful interpolation scheme for calculating the electric field components at the gravity centers of the cells, which involves both the electric displacement and the electric field utilizing the fact that the normal components of the electric displacement and the tangential components of the electric field are continuous across the particle surface.

3. Improvement on the Convergence of Near-Field Computation

In the FDTD computation, the field values in the time domain must be transformed into their counterparts in the frequency domain. If a pulse is used as the initial excitation for the time-marching iteration associated with near-field calculation in the time domain, the discrete Fourier transform is normally used to obtain the corresponding near-field signals in the frequency domain as follows:

$$F_N(\omega) = \sum_{n=0}^{N} f_n \exp(i\omega n \Delta t), \tag{24}$$

where f_n is the signal in the time domain at time step n, and $F_N(\omega)$ is the signal in the frequency domain. Note that a rigorous treatise on Fourier series and integrals was given by Sommerfeld.[20] In principle, the parameter N in Eq. (24) should be infinitely large so that a converged value of the signal in the frequency domain can be obtained. However, in practice, it must be a finite number. An interesting point to note is that the discrete Fourier transform is more

$$\frac{\partial E_z(i + 1/2, j + 1/2, k, t)}{\partial t} = \frac{c}{\varepsilon(i + 1/2, j + 1/2, k)\Delta s} [H_x(i, j - 1/2, k + 1/2, t)$$
$$- H_x(i, j + 1/2, k + 1/2, t) + H_y(i + 1/2, j, k + 1/2, t) - H_y(i - 1/2, j, k + 1/2, t)], \tag{21}$$

where

$$\varepsilon(i + 1/2, j + 1/2, k) = (\varepsilon_{i,j,k} + \varepsilon_{i+1,j,k}$$
$$+ \varepsilon_{i+1,j+1,k} + \varepsilon_{i,j+1,k})/4 . \tag{22}$$

The temporal discretization of Eq. (21), after it is transformed into a form similar to Eq. (14), is straightforward and will not produce any difficulty.

computationally efficient than the fast Fourier transform for application to the FDTD computation, as demonstrated by Furse and Gandhi.[21] This is mainly because the summation in Eq. (24) for the discrete Fourier transform can be updated at every FDTD time step in a straightforward manner, whereas the full history of the temporal variation of the signals at all grid points are required in the fast Fourier transform.

Consider the following expressions for the discrete Fourier transform with various time steps for the near-field iterations. The signals in the frequency domain are given by

$$F_{N_0}(\omega) = \sum_{n=0}^{N_0} f_n \exp(i\omega n \Delta t) , \qquad (25a)$$

$$F_{N_0+1}(\omega) = \sum_{n=0}^{N_0+1} f_n \exp(i\omega n \Delta t) , \qquad (25b)$$

$$\vdots$$

$$F_{N_0+L}(\omega) = \sum_{n=0}^{N_0+L} f_n \exp(i\omega n \Delta t) . \qquad (25c)$$

Let $F_c(\omega)$ be the converged value of $F_N(\omega)$, which, in principle, corresponds to the case with $L \to \infty$ in Eq. (25c). It is expected that $F_{N_0}(\omega)$, $F_{N_0+1}(\omega)$, $\dots F_{N_0+L}(\omega)$ will be approximately equal to $F_c(\omega)$ if N_0 is sufficiently large so that

$$F_c(\omega) = [F_{N_0}(\omega) + F_{N_0+1}(\omega) + \cdots + F_{N_0+L}(\omega)]$$
$$/(L+1) . \qquad (26)$$

Using Eqs. (25a)–(25c) and (26), we obtain

$$F_c(\omega) = \sum_{n=0}^{N_0} f_n \exp(i\omega n \Delta t) + \frac{L}{L+1} f_{N_0+1}$$
$$\times \exp[i\omega(N_0 + 1)\Delta t]$$
$$+ \frac{L-1}{L+1} f_{N_0+2} \exp[i\omega(N_0 + 2)\Delta t] + \cdots$$
$$+ \frac{1}{L+1} f_{N_0+L} \exp[i\omega(N_0 + L)\Delta t]$$
$$= \sum_{n=0}^{N_0} f_n \exp(i\omega n \Delta t) + \sum_{j=1}^{L} \frac{L+1-j}{L+1} f_{N_0+j}$$
$$\times \exp[i\omega(N_0 + j)\Delta t] . \qquad (27)$$

Physically, Eq. (27) implies that a diffusion damping term given by $(L + 1 - j)/(L + 1)$ is added to the Fourier transform after a certain time step. As we show below, the addition of the damping term to the Fourier transform substantially speeds up the convergence of the discrete Fourier transform in the FDTD computation. It should be pointed out that the present algorithm given by Eq. (27) is an empirical approach. To compare the present algorithm and its conventional counterpart given by Eq. (24), we investigate the frequency spectrum of a time-
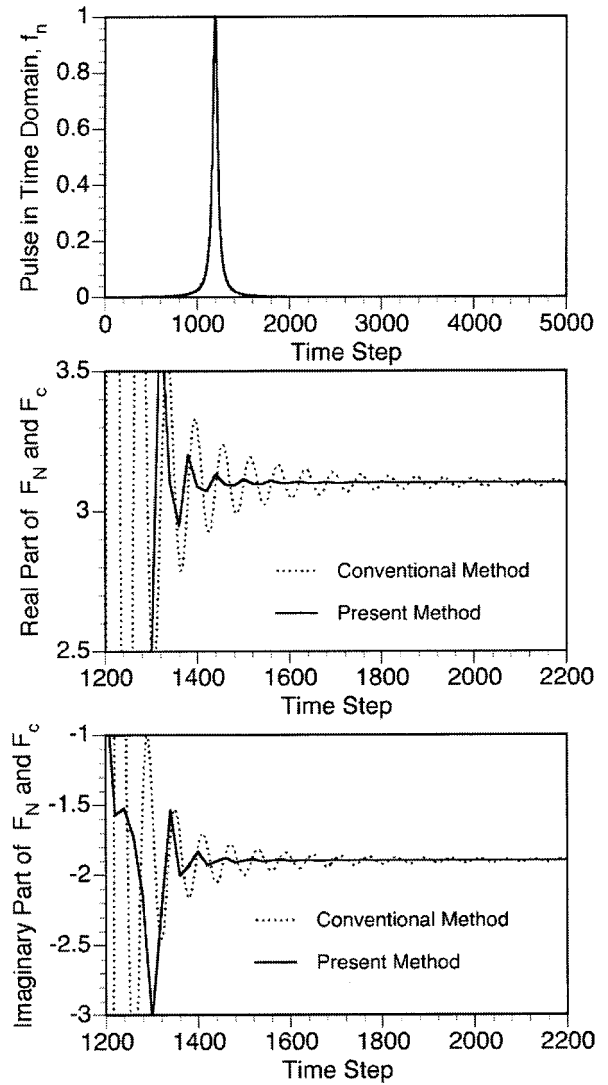

Fig. 4. Top panel: the variation of a pulse as a function of time, which is observed at the third grid point in a 1-D FDTD grid; middle panel: the real parts of $F_N(\omega)$ in Eq. (24) and $F_c(\omega)$ in Eq. (26); bottom panel: the imaginary parts of $F_N(\omega)$ and $F_c(\omega)$.

dependent pulse as a canonical problem, which is specified as follows:

$$f_n = \frac{1}{0.001(n - 1000)^2 + 1} . \qquad (28)$$

We simulate the propagation of this pulse using a one-dimensional FDTD scheme. Note that, for a one-dimensional FDTD scheme, an exact absorbing boundary condition can be constructed. In the simulation, the source is located at the third grid point. We sample the time series of the signals at the 100th grid point to perform the Fourier transform for a frequency of $\omega = 2\pi c/(30\Delta s)$ in which Δs is the grid size and c is the speed of light. The upper panel of Fig. 4 shows the pulse as a function of time step, which is observed in the third grid point. The middle and lower panels show the real and imaginary
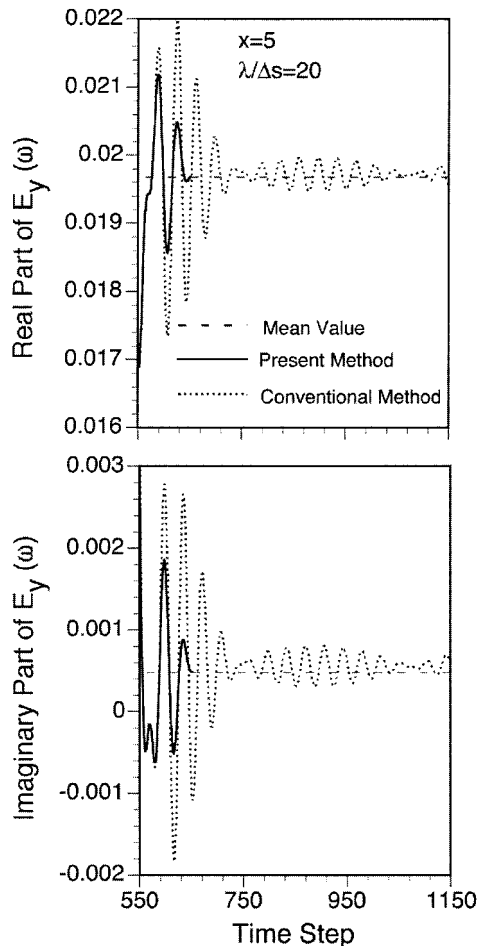
Fig. 5. Variation of the y component of the electric field at the center of a sphere versus the time step used for the Fourier transform to derive the field signals in the frequency domain. The sphere is illuminated by a y-polarized incident pulse that propagates along the z axis. The complex refractive index for the scattering particle is $m = 1.0925 + i0.248$.
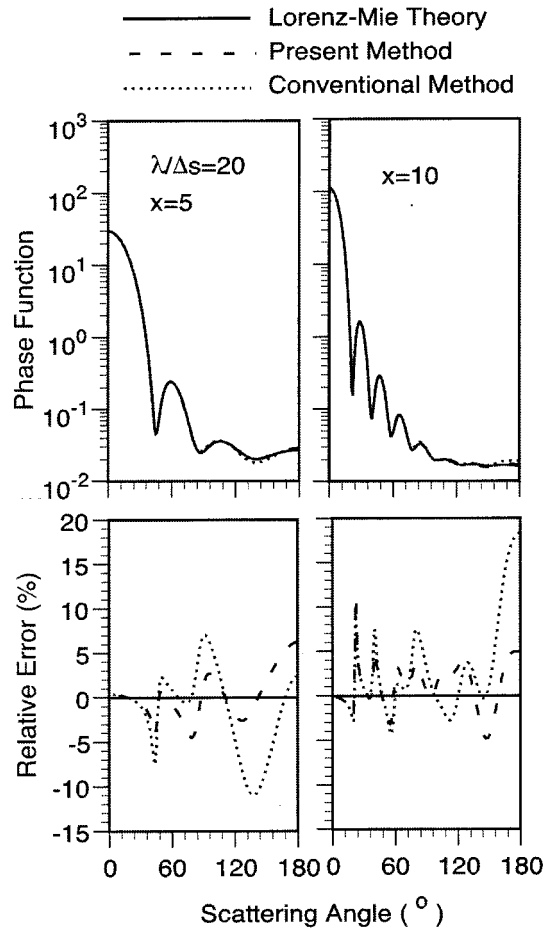

Fig. 6. Phase functions computed from the FDTD technique with the modified Fourier-transform method given by Eq. (27) and the conventional Fourier-transform method by Eq. (24), which are compared with their Lorenz–Mie counterparts. The complex refractive index for the scattering particle is $m = 1.0925 + i0.248$.

parts of the signal in the frequency domain, respectively. In the computation, we select $L = 120$ in Eq. (27). Evidently, the present algorithm leads to a fast convergence for the signals in the frequency domain.

Figure 5 shows the real and imaginary parts of the y component of the electric field (in the frequency domain) at the center of a sphere that is illuminated by a y-polarized incident pulse propagating along the z axis. In the present computation concerning electromagnetic scattering by a dielectric particle, the incident pulse is defined as follows:

$$f_n = \exp[-(n/30 - 5)^2]. \qquad (29)$$

Note that the values of the field signals shown in Fig. 5 are not normalized by the Fourier transform of the incident wave. The refractive index for the sphere is $1.0925 + i0.248$, the refractive index of ice at a wavelength of $11\,\mu$m. We employ an eight-layer perfectly matched layer boundary condition[22] with ten cells between the scattering particle and the perfectly

matched layer medium throughout the present FDTD simulation. The dotted curves in Fig. 5 are the near-field values in the frequency domain that are calculated by the conventional Fourier-transform technique given by Eq. (24). A slow convergence is evident for this conventional technique as oscillations are still noticeable when N in Eq. (24) is as large as 1150. The solid curves in Fig. 5 are the solutions given by Eq. (27) with $L = 87$. The convergence of the modified Fourier-transform scheme is observed at $N_0 = 565$ (i.e., with a total iteration step of 653). It is evident that the diffusion damping term introduced into Eq. (27) substantially improves the speed of the convergence. The dashed curves in Fig. 5 indicate the converged values predicted from Eq. (27).

Figure 6 shows the phase functions of ice spheres for a wavelength of $11\,\mu$m for size parameters $x = 5$ and 10. The size parameter is defined as $x = 2\pi a/\lambda$, where a is the radius and λ is the wavelength. For the case with $x = 5$, the total iteration steps for the calculation of the near field in the time domain is 653. When Eq. (27) is applied to the Fourier transform, the

field values between 566 and 653 are averaged, i.e., $L = 87$ in Eq. (27). Use of the average values for the fields, accuracy for the phase function in the scattering angles near 140° is much improved, although errors are slightly enhanced around the backscattering direction. For the case of $x = 10$, the total number of iteration time steps is 2173. For the modified Fourier-transform scheme given in Eq. (27), $N_0 = 2030$ and $L = 143$ are used. It is evident from the panels on the right-hand side of Fig. 6 that the maximum error for the phase-function calculation can be as large as 20% when 2173 time steps are used for the time-marching iteration of the near-field calculation. However, accuracy for the phase function calculation is substantially increased if the field values are averaged in the Fourier transform even though the same time steps are used.

4. Comparison of Two Finite-Difference Time-Domain Numerical Schemes

In this section we compare the numerical accuracy of two FDTD schemes that are associated with the grid configurations shown in Figs. 1(a) and 1(b). Throughout the present computations, the cells in the vicinity of the particle surface are defined as empty cells (i.e., with $\varepsilon = 1$) if 50% of the cell volume is outside the particle. If more than half of a cell is inside the particle, the dielectric properties (i.e., the real and imaginary parts of permittivity) of the particle are assigned to the cell. For numerical simplicity, the effective permittivity calculated on the basis of the Maxwell Garnett rule or the Bruggeman rule, which is suggested by Yang et al.[9] for the cells at the particle surface, is not used in this study.

Figure 7 shows a comparison of the phase function for an ice sphere with a size $x = 5$ at a far-infrared (IR) wavelength of 25 μm. Note that there is an increasing interest in use of the far-IR spectral signature to retrieve the microphysical and optical properties of ice clouds.[23] The refractive index of ice at this wavelength is $1.5015 + i0.067$. In the numerical computation, 1984 time steps are used for the near-field iteration. The field values for the last 420 time steps are averaged in the Fourier transform based on Eq. (27). In the following we refer to the scheme associated with the grid configuration in Fig. 1(a) as scheme 1 and that in Fig. 1(b) is referred to as scheme 2. As shown in Fig. 7, accuracy is similar for these two FDTD schemes, although scheme 2 gives larger errors near the backscattering directions.

Figure 8 is the same as Fig. 7, except for a size parameter of $x = 10$. For this size parameter, 5872 steps of the time-marching iterations are carried out to obtain the near-field in the frequency domain. The overall performances of these two schemes are quite similar. However, scheme 1 is more accurate for the phase–function calculations for scattering angles near 180°, whereas scheme 2 is slightly better near 150°.

It is quite challenging to accurately determine the optical properties of a dielectric particle having a large refractive index, as articulated by Sun and Fu[11]
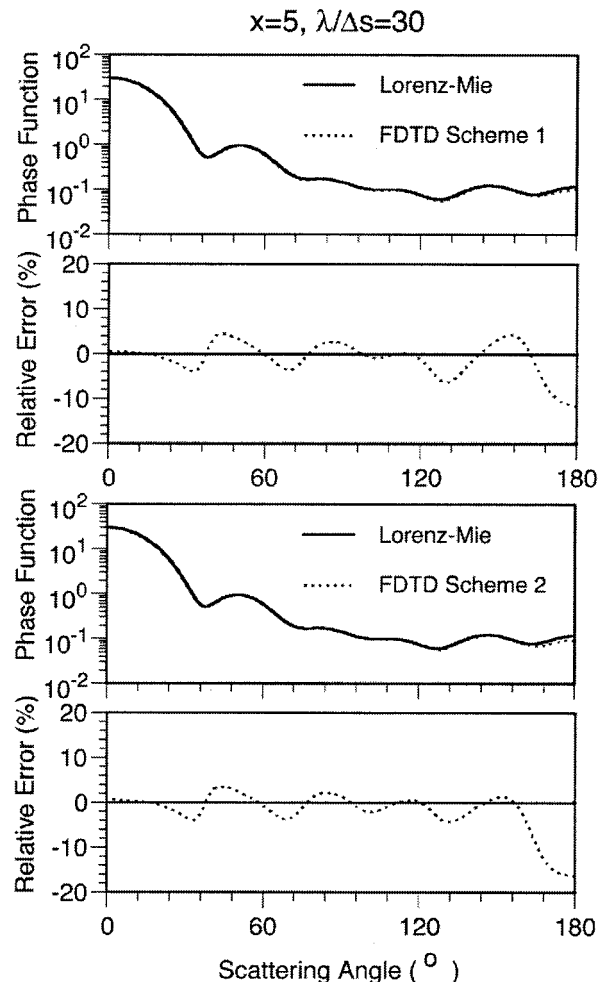

Fig. 7. Phase functions computed by use of the two grid configurations shown in Figs. 1(a) and 1(b). Also shown are the relative errors in comparison with Lorenz–Mie theory. The complex refractive index for the scattering particle is $m = 1.5015 + i0.067$.

who applied the FDTD technique to cases with refractive indices as large as $(7.1499 + i2.914)$. They showed that an interpolation involving the electric displacement is necessary in the case in which the refractive index is large. In this study we calculate the electric field components, say E_z, by directly averaging the four E_z values at cell edges when scheme 1 is used. For scheme 2, an electric field component, say E_z, is given by Eq. (20). Figure 9 shows the phase functions calculated from the two schemes. The complex refractive index used in the calculation is $8.2252 + i1.6808$, the refractive index of water (at a temperature of 300 K) at a microwave wavelength of 3.2 cm. Because the refractive index is large in this case, a fine grid resolution ($\lambda/\Delta s = 165$) is necessary to resolve the sharp gradient of the near-field inside the particle. For the results computed from both schemes, the total time-marching iterations required are 7500 steps. For scheme 1, the relative error is of the order of 5%; the maximum error occurs for backscattering. The error pattern for scheme 2
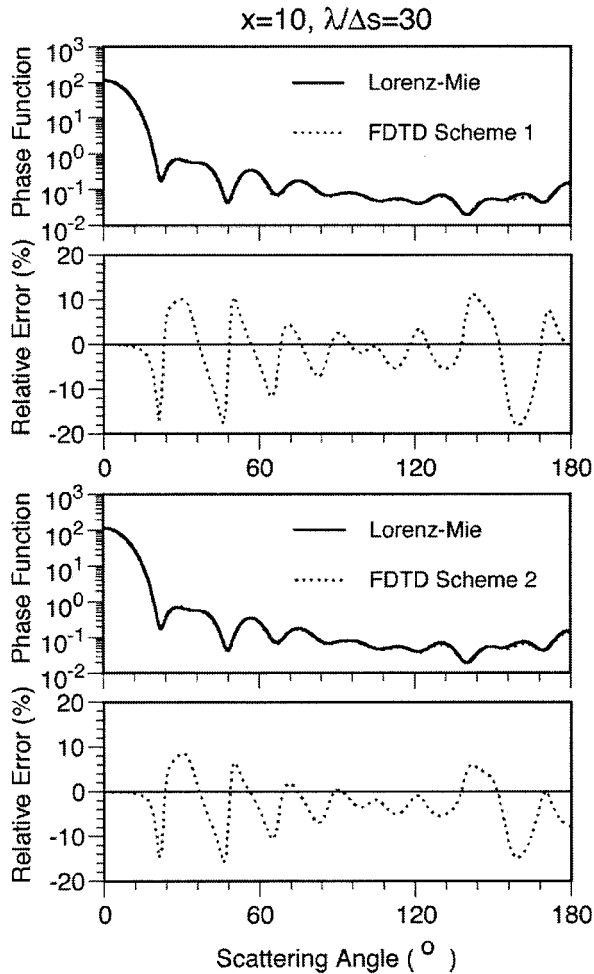
x=10, λ/Δs=30

x=5, λ/Δs=165

Fig. 8. Same as Fig. 7, except for a size parameter of $x = 10$.

Fig. 9. Comparison of the two FDTD schemes for a case with a large refractive index ($m = 8.2252 + i1.6808$).

is quite similar to that for scheme 1 although its error is larger in the backscattering directions. Evidently, the performance of schemes 1 and 2 are quite similar although different averaging methods are used to evaluate the permittivity at the locations where the dielectric properties of the media are not continuous.

Figure 10 shows the phase functions calculated from the two FDTD schemes for cubic particles that are assumed to be randomly oriented in space. Also shown in Fig. 10 are the relative errors that are defined as [solution(scheme1) − solution(scheme2)/ solution(scheme1)]. Following Chamaillard *et al.*,[24] the refractive index of sea-salt aerosols ($1.5 + i10^{-8}$) at a wavelength of 0.55 μm is used here. As illustrated from the scanning electron photograph, the shape of sea-salt aerosols can be cubic.[24] Because there is no exact reference phase function for this case, we are unable to identify whether scheme 1 or scheme 2 is more accurate; however, we can compare the differences between the two. From Fig. 10, the differences between the two schemes, in the phase-function calculation, are of the order of a few percent
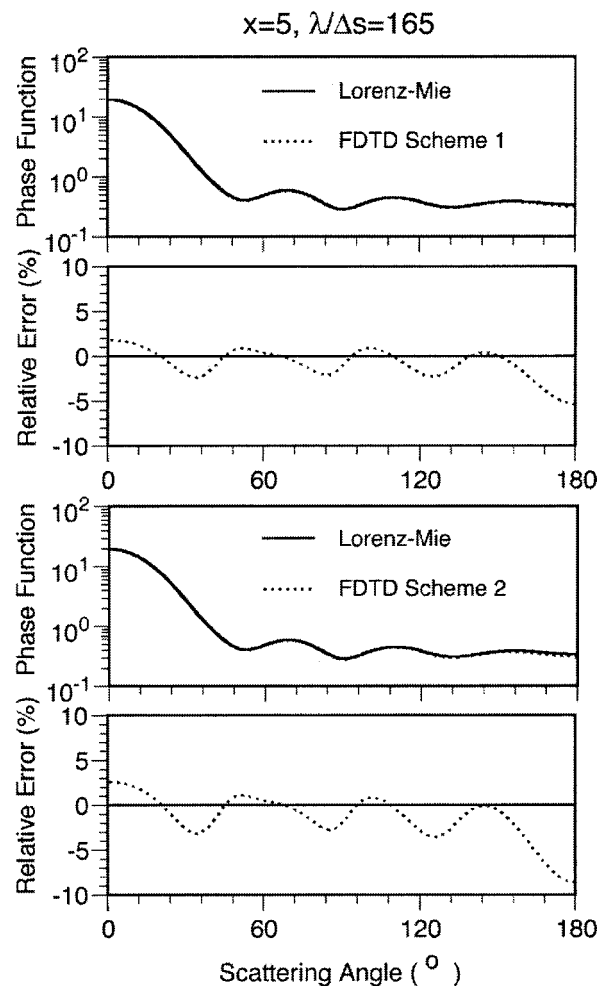
with larger differences occurring in the backscattering directions.

As a new application of the FDTD method, we calculated the scattering phase matrix of bullet-rosette ice crystals that are assumed to be randomly oriented in space. These ice crystals have various branches and are often observed in ice clouds.[25,26] The single-scattering properties of these types of ice crystal are fundamental to radiative transfer calculations and remote sensing applications involving cirrus clouds. The geometric-optics method has been employed by Iaquinta et al.[25] to investigate the phase functions of multibranched bullet rosettes. The scattering properties of bullet rosettes with four and six branches have also been studied by Yang and Liou using the FDTD and geometric-optics methods.[27,28] In this study we further investigate the effect of multibranch bullet rosettes on the scattering and absorption properties of these ice crystals. Figure 11 shows the bullet-rosette geometries with 1, 3, 4, 5, 6, 8, 9, 10, and 12 branches. For simplicity in numerical computation, we assume that all the branches are identical. The tip of an individual bullet element is one
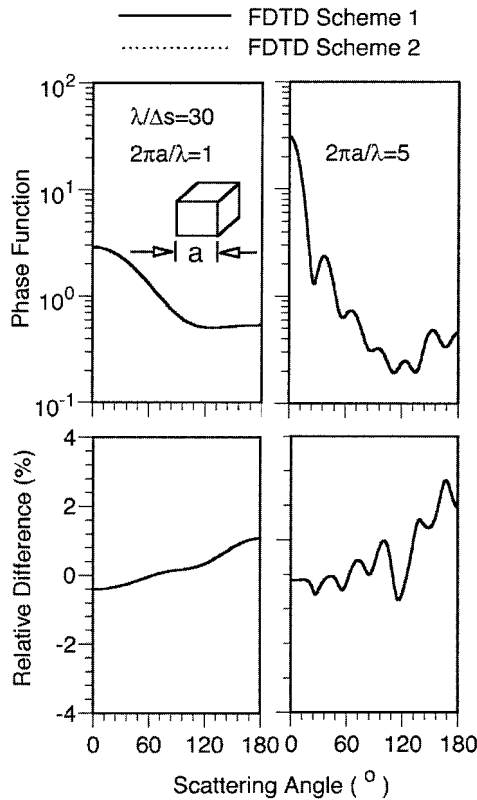
Fig. 10. Comparison of the two FDTD schemes for light-scattering computations involving cubic particles. Note that the solid and dotted curves in the upper panels are essentially overlapped. The refractive index of sea-salt aerosols, $m = 1.5 + i10^{-8}$, is used in the computation.
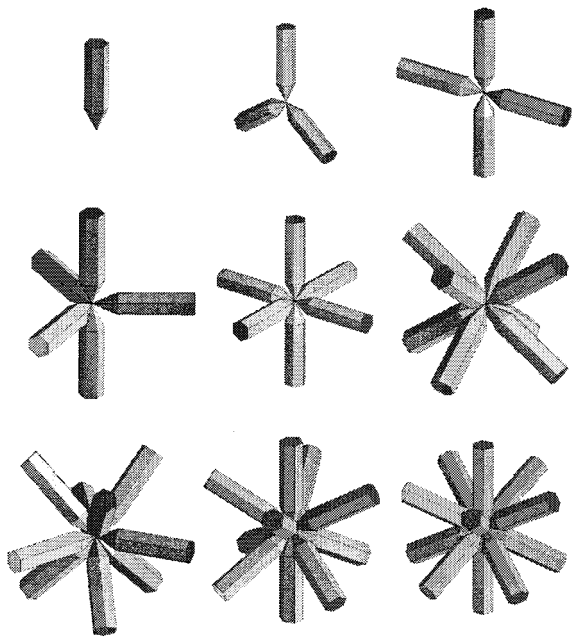

Fig. 11. Morphological geometry of bullet-rosette ice crystals defined for scattering calculations.
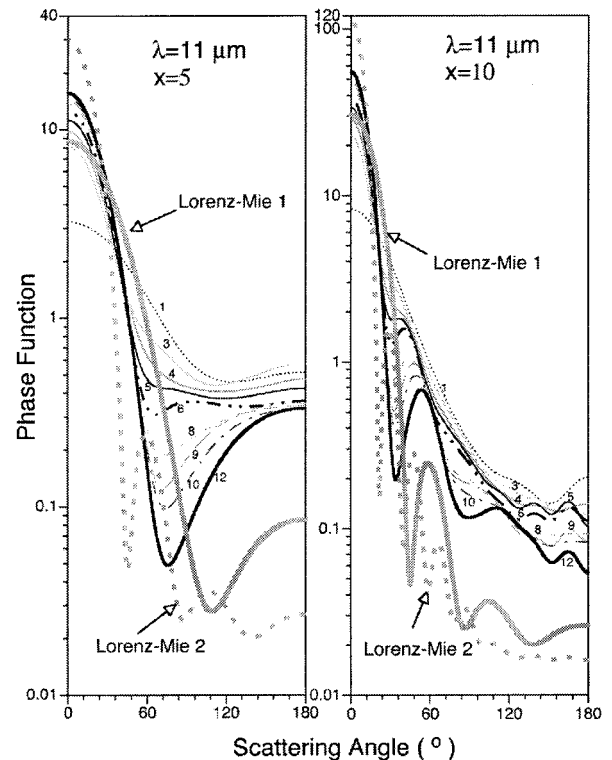

Fig. 12. Phase functions of bullet-rosette ice crystals with 1–12 branches. The wavelength is 11 μm. The size parameter for the particle is defined as $x = 5$, where $x = 2\pi D/\lambda$ and D is the length of a bullet element. The complex refractive index for the scattering particle is $m = 1.0925 + i0.248$. The term Lorenz–Mie 1 refers to the results for the spheres that have the same volume as the bullet-rosette ice crystals with 12 branches, whereas the term Lorenz–Mie 2 refers to the results for the spheres that have the same diameters as the bullet-rosette ice crystals.

fifth of the total length of the element. The angle between the pyramidal faces of a bullet element and its axis is 26.5°. In the present light-scattering computation, the bullet-rosette ice crystals are assumed to be randomly oriented in space. Note that the tips of the bullet geometry defined in this study differ from those reported by Iaquinta et al.[25]

Figure 12 shows the phase functions of bullet-rosette ice crystals with size parameters of $x = 5$ and 10, where $x = 2\pi D/\lambda$ and D is the length of an individual bullet element. The FDTD scheme associated with the grid configuration in Fig. 1(a) is used for this calculation. The wavelength for the results shown in Fig. 12 is 11 μm and the corresponding refractive index is (1.0925 + i0.248). For comparison, we also show the phase functions of circumscribing spheres, i.e., the spheres with the same dimensions as the bullet rosettes. In addition, we present the phase functions of the ice spheres that have the same volumes as the bullet rosettes with 12 branches. Note that the size parameters of the equivalent-volume spheres are 2.523 and 5.046 for the results shown in the left and right panels of Fig. 12, respectively. The left panel of Fig. 12 shows the case for $x = 5$. Evidently, the phase-function values

Table 1. Extinction Efficiency (Q_e), Single-Scattering Albedo ($\tilde{\omega}$), and Asymmetry Factor (g) for Bullet-Rosette Ice Crystals Associated with the Phase Functions Shown in Fig. 12[a]

Branches	$x = 5$			$x = 10$		
	Q_e	$\tilde{\omega}$	g	Q_e	$\tilde{\omega}$	g
1	0.5723	0.0758	0.3602	0.9535	0.2001	0.6283
3	0.5450	0.0902	0.4316	0.9429	0.2096	0.6712
4	0.5671	0.1004	0.5014	0.9632	0.2189	0.7023
5	0.5855	0.1088	0.5443	0.9750	0.2285	0.7200
6	0.6359	0.1224	0.5899	1.0101	0.2391	0.7475
8	0.6431	0.1380	0.6489	1.0542	0.2562	0.7881
9	0.6318	0.1417	0.6681	1.0486	0.2631	0.7987
10	0.6638	0.1529	0.6964	1.0734	0.2724	0.8111
12	0.6957	0.1667	0.7354	1.1071	0.2863	0.8309

[a]x is the size parameter defined as $x = 2\pi D/\lambda$.

near the forward-scattering direction increases with the number of bullet branches because the particle volume is proportional to the branch number. An interesting feature to note is that the scattering minima of the phase function in the side-scattering direction decreases with an increase in the branch number and shifts toward larger scattering angles. The overall phase-function pattern for the circumscribing spheres differ substantially from those for bullet-rosette ice crystals. In particular, two scattering maxima can be seen in the spherical case, which are absent in the case for bullet rosettes. For the equivalent-volume sphere, the overall phase-function pattern is similar to those for the nonspherical particles, but detailed differences are still noticeable. The right panel of Fig. 12 is the case of $x = 10$. In this case, we also note that the number of bullet branches has a significant effect on the phase-function pattern. For bullet rosettes with 8, 9, 10, and 12 branches, there are pronounced scattering maxima in the side-scattering direction. As can be seen for the case of $x = 5$, the phase functions for the spheres in the right panel of Fig. 12 are also quite different from those of bullet rosettes. It is clear from Fig. 12 that an equivalent substitute in the phase-function calculation does not exist for complex particle geometries. Chou *et al.*[29] show that the scattering effect of cloud particles are nonnegligible even in the IR spectral region. Figure 12 illustrates that bullet-rosette ice crystals have much stronger side scattering ($>120°$) and backscattering. These scattering features could have implications in atmospheric radiative transfer computations involving cirrus clouds.

Table 1 lists the extinction efficiency, single-scattering albedo, and asymmetry factor associated with the phase functions shown in Fig. 12. We note that the values of these three quantities are monotonically increasing with increasing branch number.

Figures 13 and 14 show the nonzero elements of the scattering phase matrix at a wavelength of 0.66 μm for bullet rosettes with 1, 6, and 12 branches for size parameters $x = 5$ and 10, respectively. The complex refractive index of ice for this wavelength is $1.3078 + i1.66 \times 10^{-8}$ based on the data compiled by

Warren.[30] The nonzero phase-matrix elements of the spheres with the same volume as the 12-branched bullet rosettes are also shown. The nonsphericity effect on the phase-matrix elements is evident from these two diagrams. It has been suggested that P_{22}/P_{11} is indicative of nonsphericity[19,31] because this ratio is unity for a sphere. From Figs. 13 and 14, the nonsphericity in terms of the deviation of P_{22}/P_{11} from unity becomes more significant with increasing branch number. The other phase-matrix elements for bullet rosettes are also quite different from those for spheres. We note that the elements P_{12}/P_{11}, P_{33}/P_{11}, P_{43}/P_{11}, and P_{44}/P_{11} are not particularly
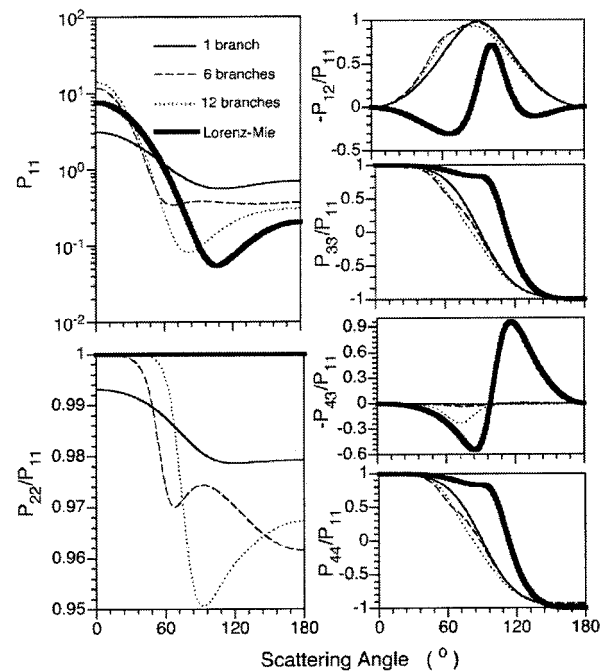

Fig. 13. Nonzero phase-matrix elements for the bullet-rosette ice crystals with 1, 6, and 12 elements for a wavelength of 0.66 μm at which the refractive index of ice is $1.3078 + i1.66 \times 10^{-8}$. The size parameter is $x = 5$. The phase-matrix elements of a sphere that has the same volume as the 12-branched bullet rosettes are also shown.
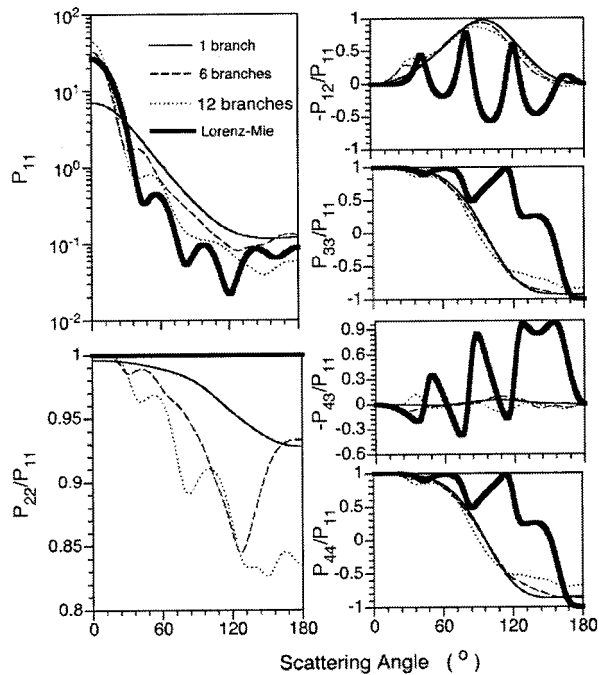
Fig. 14. Same as Fig. 13, except for $x = 10$.

sensitive to the number of branches in bullet rosettes. Finally, we point out that for pure backscattering, the calculated phase matrices presented herein satisfy the reciprocity relation,[2] namely,

$$1 - P_{22}/P_{11} = P_{44}/P_{11} - P_{33}/P_{11}. \qquad (30)$$

This result is quite general and holds for a particle in a fixed orientation or in random orientations.

5. Conclusions

In the Cartesian FDTD grid configuration that was originally reported by Yee in 1966, the electric field components were defined at cell edges, whereas the magnetic field components were defined at cell-face centers. This configuration automatically satisfies the electromagnetic boundary condition if a scattering dielectric particle is represented by a number of homogeneous cubic cells in the FDTD computation. Alternatively, the electric field components can be defined at the center of cell faces, whereas the magnetic field components can be specified at cell edges. When the permittivity values of adjacent cells are different, they are not defined at cell edges or face centers in both grid configurations. In this study we suggest two numerical schemes to overcome the discontinuity of the permittivities for nonidentical adjacent cells on the basis of the electromagnetic boundary conditions. Furthermore, we show that, if the electric field components are defined at the centers of cell faces, the electric field components involved in the finite-difference analog of Maxwell's equations are the averages of the electric field values at two different sides of the cell interface. The present FDTD schemes associated with the grid con-

figurations in Figs. 1(a) and 1(b) have been applied to light scattering by dielectric spheres with a moderate and a large refractive index. In general, the performance of these two FDTD schemes is similar. The important point to note is that, from first principles, an average of permittivity is inevitable in the Cartesian FDTD scheme regardless of the specific grid configuration.

We also find that the field values in the frequency domain, which are derived from the discrete Fourier-transform technique, converge extremely slowly. A simple yet efficient empirical approach has been developed to accelerate the convergence rate. In a case study involving the refractive index for ice at a wavelength of 11 μm, the errors associated with the modified Fourier-transform method are significantly reduced, as compared with those derived from the conventional Fourier transform.

Finally, we investigate the effect of multiple branches of bullet-rosette ice crystals on the single-scattering properties of these ice crystals by using the FDTD method. Numerical results illustrate that their scattering properties are dependent on the number of bullet elements. We also show that the approximation in which equivalent spheres are used to simulate complex bullet rosettes leads to significant errors in the phase-function calculation.

References

1. K. N. Liou, *Introduction to Atmospheric Radiation* (Academic, San Diego, Calif., 2002).
2. M. I. Mishchenko, J. W. Hovenier, and L. D. Travis, eds., *Light Scattering by Nonspherical Particles* (Academic, San Diego, Calif., 2000).
3. F. M. Kahnert, "Numerical methods in electromagnetic scattering theory," J. Quant. Spectrosc. Radiat. Transfer **79–80,** 775–824 (2003).
4. K. S. Yee, "Numerical solution of initial boundary problems involving Maxwell's equations in isotropic media," IEEE Trans. Antennas Propagat. **AP-14,** 302–307 (1966).
5. A. Taflove, *Advances in Computational Electromagnetics* (Artech House, Boston, Mass., 1998).
6. A. Taflove and S. C. Hagness, *Computational Electromagnetics*, 2nd ed. (Artech House, Boston, Mass., 2000).
7. K. S. Kunz and R. J. Luebbers, *The Finite Difference Time Domain Method for Electromagnetics* (CRC Press, Boca Raton, Fla., 1993).
8. P. Yang and K. N. Liou, "Finite-difference time domain method

for light scattering by small ice crystals in three-dimensional space," J. Opt. Soc. Am. A **13,** 2072–2085 (1996).

9. P. Yang, K. N. Liou, M. I. Mishchenko, and B.-C. Gao, "An efficient finite-difference time domain scheme for light scattering by dielectric particles: application to aerosols," Appl. Opt. **39,** 3727–3737 (2000).

10. W. Sun, Q. Fu, and Z. Chen, "Finite-difference time-domain solution of light scattering by dielectric particles with perfectly matched layer absorbing boundary conditions," Appl. Opt. **38,** 3141–3151 (1999).

11. W. Sun and Q. Fu, "Finite-difference time-domain solution of light scattering by dielectric particles with large complex refractive indices," Appl. Opt. **39,** 5569–5578 (2000).

12. K. Aydin, "Centimeter and millimeter wave scattering from nonspherical hydrometeors," in *Light Scattering by Nonspherical Particles*, M. I. Mishchenko, J. Hovenier, and L. D. Travis, eds. (Academic, San Diego, Calif., 2000), pp. 451–479.

13. K. Aydin and C. Tang, "Millimeter wave radar from model ice crystal distributions," IEEE Trans. Geosci. Remote Sens. **35,** 140–146 (1997).

14. S. C. Hill, G. Videen, W. B. Sun, and Q. Fu, "Scattering and internal fields of a microsphere that contains a satiable absorber: finite-difference time domain simulations," Appl. Opt. **40,** 5487–5494 (2001).

15. K. L. Shlager and J. B. Schneider, "A survey of the finite-difference time domain literature," in *Advances in Computational Electrodynamics*, A. Taflove, ed. (Artech House, Boston, Mass., 1998), pp. 1–62.

16. T. G. Jurgens, A. Taflove, K. Umashankar, and T. G. Moore, "Finite-difference time domain modeling of curved surfaces," IEEE Trans. Antennas Propagat. **40,** 357–366 (1992).

17. R. Pregla and W. Pascher, "The method of lines," in *Numerical Techniques for Microwave and Millimeter-Wave Passive Structure*, T. Itoh, ed. (Wiley, New York, 1989), pp. 381–446.

18. C.-T. Tai, *Dyadic Green Functions in Electromagnetic Theory*, 2nd ed. (Institute of Electrical and Electronics Engineers New York, 1994).

19. M. I. Mishchenko, L. D. Travis, and A. A. Lacis, *Scattering, Absorption, and Emission of Light by Small Particles* (Cambridge U. Press, Cambridge, UK, 2002).

20. A. Sommerfeld, *Partial Differential Equations in Physics* (Academic, New York, 1949).

21. C. M. Furse and O. P. Gandhi, "Why the DFT is faster than the FFT for FDTD time-to-frequency domain conversions," IEEE Microwave Guid. Wave Lett. **5,** 326–328 (1995).

22. J. P. Berenger, "A perfect matched layer for the absorption of electromagnetic waves," J. Comput. Phys. **114,** 185–200 (1994).

23. P. Yang, M. G. Mlynczak, H. L. Wei, D. P. Kratz, B. A. Baum, Y. X. Hu, W. J. Wiscombe, A. Heidinger, and M. I. Mishchenko, "Spectral signature of cirrus clouds in the far-infrared region: single-scattering calculation and radiative sensitivity study," J. Geophys. Res. **108D,** 4569, 10.1029/2002JD003291 (2003).

24. K. Chamaillard, S. G. Jennings, C. Kleefeld, D. Ceburnis, and Y. J. Yoon, "Light backscattering and scattering by nonspherical sea-salt acrosols," J. Quant. Spectrosc. Radiat. Transfer **79–80,** 577–597 (2003).

25. J. Iaquinta, H. Isaka, and P. Personne, "Scattering phase functions of bullet rosette ice crystals," J. Atmos. Sci. **52,** 1401–1413 (1995).

26. A. J. Heymsfield and J. Iaquinta, "Cirrus crystal terminal velocities," J. Atmos. Sci. **57,** 916–938 (2000).

27. P. Yang and K. N. Liou, "Finite difference time domain method for light scattering by nonspherical and inhomogeneous particles," in *Light Scattering by Nonspherical Particles*, M. I. Mishchenko, J. W. Hovenier, and L. D. Travis, eds. (Academic, San Diego, Calif., 2000), pp 174–221.

28. P. Yang and K. N. Liou, "Single-scattering properties of complex ice crystals in terrestrial atmosphere," Contrib. Atmos. Phys. **71,** 223–248 (1998).

29. M. D. Chou, K. T. Lee, S.-C. Tsay, and Q. Fu, "Parameterization for cloud longwave scattering for use in atmospheric models," J. Clim. **12,** 159–169 (1999).

30. S. Warren, "Optical constants of ice from ultraviolet to the microwave," Appl. Opt. **23,** 1206–1225 (1984).

31. C. F. Bohren and D. R. Huffman, *Absorption and Scattering of Light by Small Particles* (Wiley, New York, 1983).